Electronic Supplementary Material (ESI) for Journal of Materials Chemistry A.

— Electronic Supplementary Information —

Controlling thermoelectric transport via native defects in the diamond-like semiconductors $Cu_2HgGeTe_4$ and Hg_2GeTe_4

Jiaxing Qu,[†] Claire E. Porter,[‡] Lídia C. Gomes,[†] Jesse M. Adamczyk,[‡] Michael Y. Toriyama,[¶] Brenden R. Ortiz,[§] Eric S. Toberer,[‡] and Elif Ertekin[*,†]

[†]*University of Illinois at Urbana-Champaign, Urbana, IL 61801*

[‡]*Colorado School of Mines, Golden, CO 80401*

[¶]*Northwestern University, Evaston, IL 60208*

[§]*University of California Santa Barbara, Santa Barbara, CA 93106*

E-mail: ertekin@illinois.edu

1. X-ray diffraction patterns for Hg_2GeTe_4

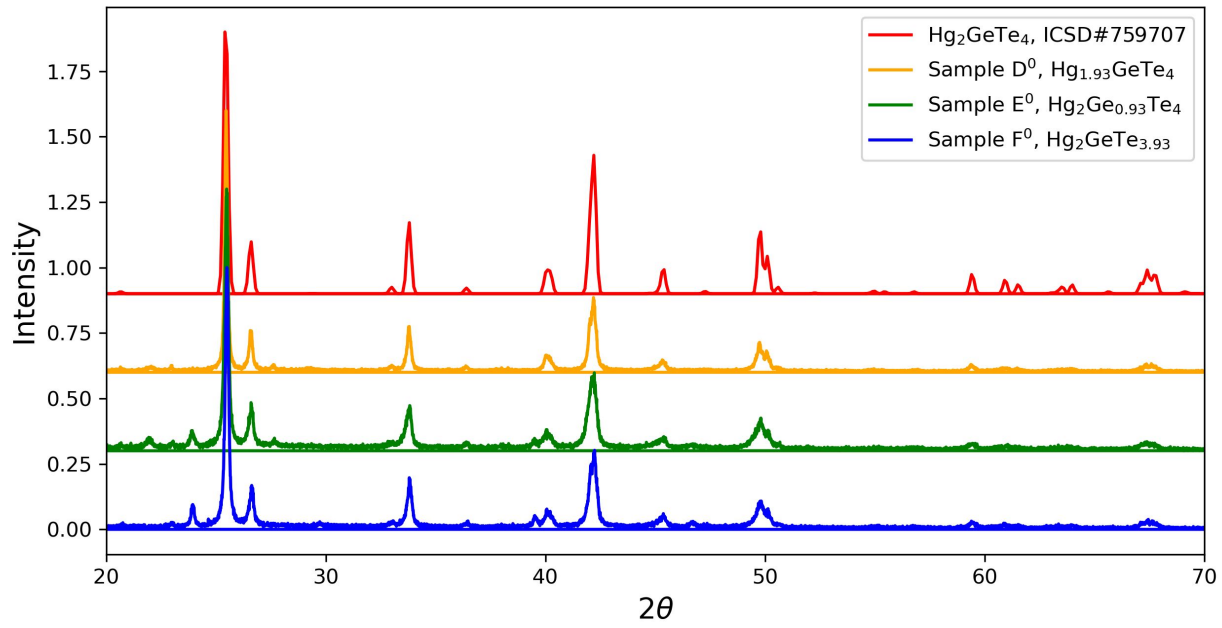

Figure S1: XRD patterns of ternary samples shown with ICSD data for Hg_2GeTe_4 (red). The small peak observed at $2\theta = 24.1°$ for samples E^0 (green) and F^0 (blue) corresponds with trace amounts of HgTe.

2. Schematic for band edge shifts for $Cu_2HgGeTe_4$ and Hg_2GeTe_4

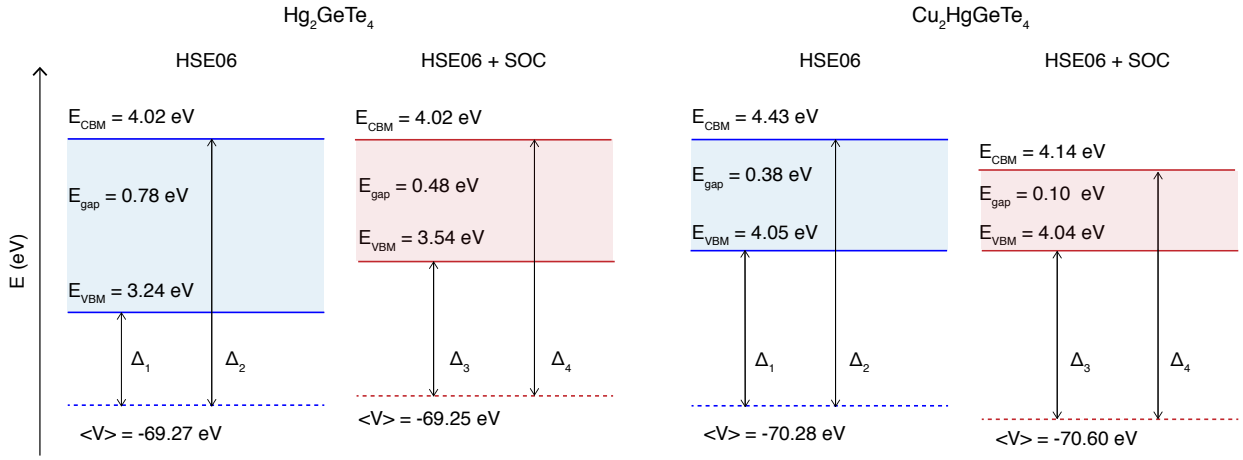

Figure S2: Schematic of band edge shifts for $Cu_2HgGeTe_4$ and Hg_2GeTe_4 by comparing energies from HSE06 and HSE06+SOC. Here $\langle V \rangle$ represents average electrostatic potential, Δ_1 (or Δ_2) correspond to energy difference between $\langle V \rangle$ and valence band maximum (VBM) (or conduction band minimum (CBM)) calculated using the HSE06 hybrid functional. Similarly, Δ_3 (or Δ_4) correspond to the energy difference between $\langle V \rangle$ and the VBM (or CBM) calculated using HSE06 with spin-orbit coupling effects. The band edge shifts for the VBM is obtained by Δ_1-Δ_3, and band edge shifts for the CBM by Δ_2-Δ_4.

3. Density-of-states for $Cu_2HgGeTe_4$ and Hg_2GeTe_4

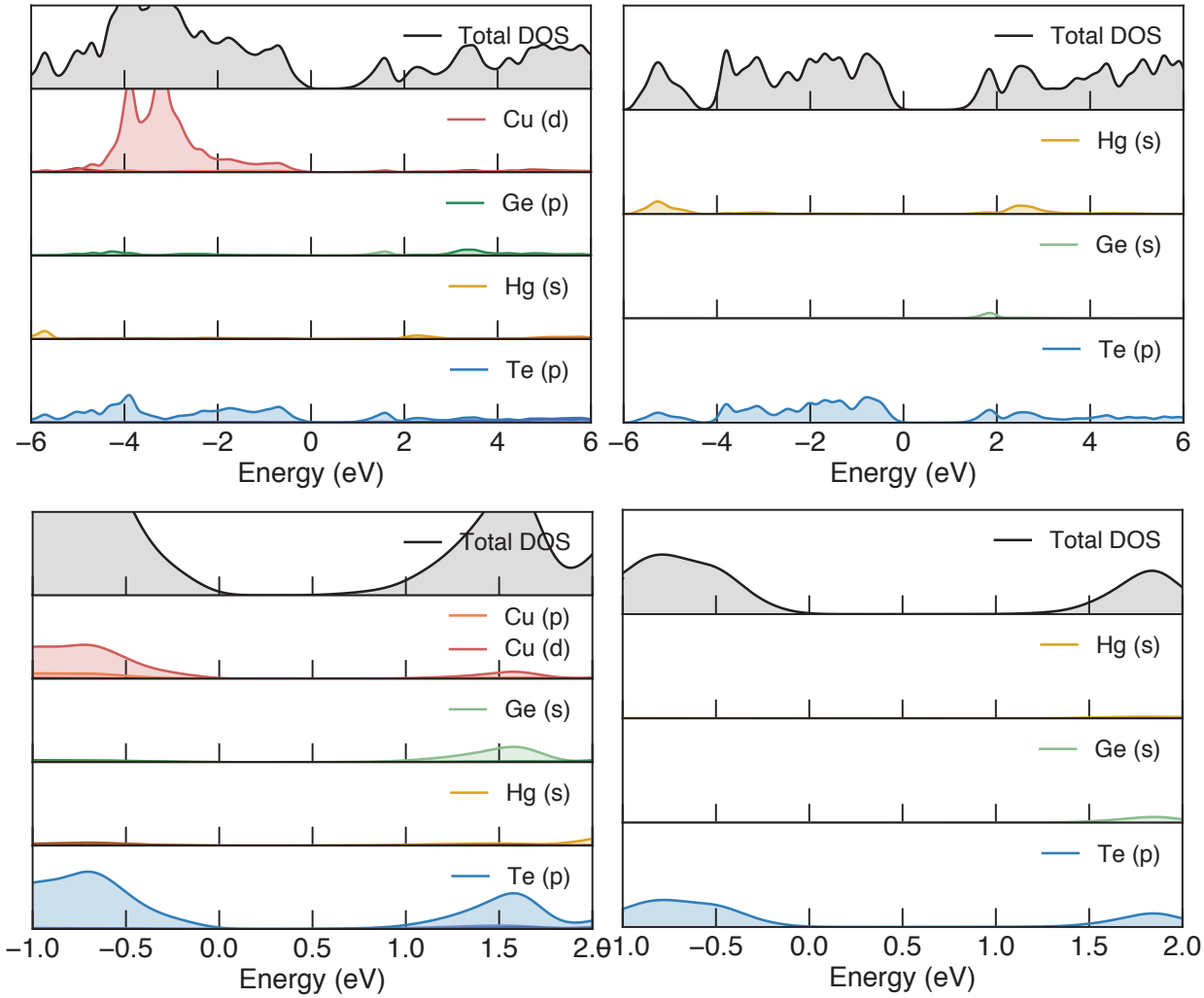

Figure S3: Total and partial density-of-states (DOS) calculated for $Cu_2HgGeTe_4$ and Hg_2GeTe_4 using tetrahedron method obtained from HSE06 hybrid functional, for a wide energy window (top) and zoomed-in window around band edges (bottom). DOS is plotted using the Sumo [1] python toolkit and post-processed using Gaussian smearing.

4. Defect diagrams for Cu-doped Hg_2GeTe_4

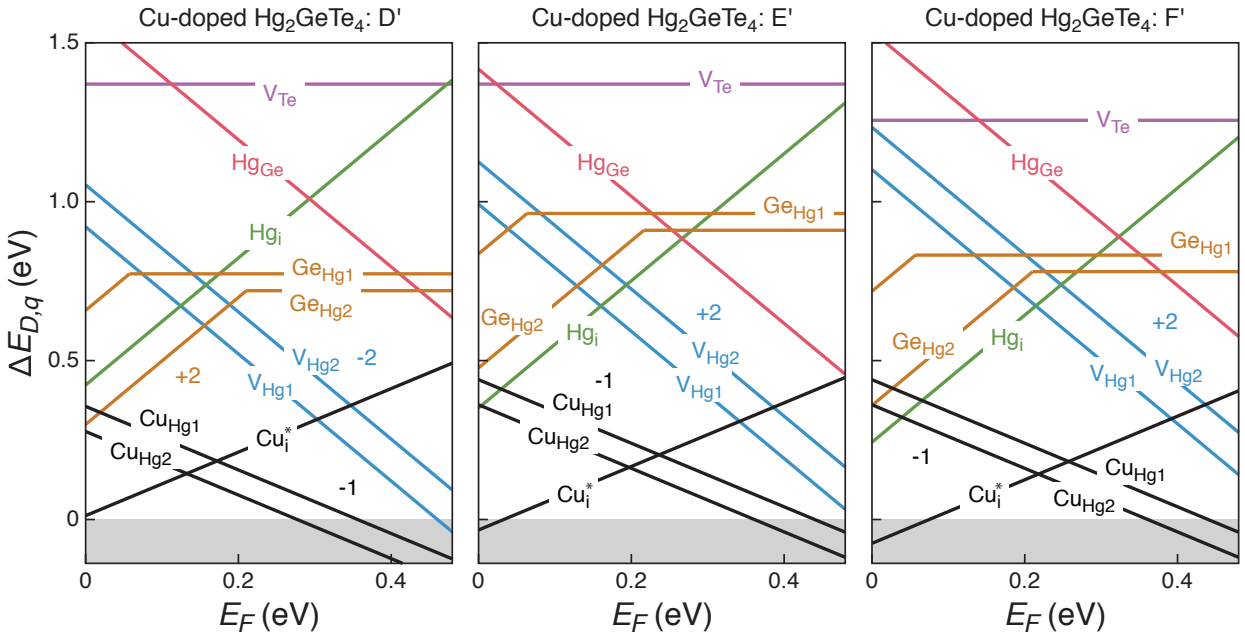

Figure S4: Defect formation energy for native point defects as a function of Fermi energy in Cu-doped Hg_2GeTe_4 at growth condition D', E' and F', calculated with HSE06 and band edge shifts from HSE06+SOC. The effective Fermi energy E_F^{eff} lies around the VBM, located at -0.03, 0.0 and 0.01 eV reference to VBM for D', E' and F' growth condition respectively.

5. Predicted thermoelectric performance of $Cu_2HgGeTe_4$ and Hg_2GeTe_4 evaluated using quality factor β

Table S1: Computed transport properties and thermoelectric performance calculated using the HSE06 hybrid functional. Here, β values are normalized by the p- and n-type β of PbTe, m_b^* is the band effective mass, N_b is the conduction band degeneracy, μ is the room temperature electron mobility and κ_L is the room temperature lattice thermal conductivity. κ_L and μ are calculated using semi-empirical models from Ref. 2. The predicted value for κ_L is larger than the experimentally measured value, particularly for $Cu_2HgGeTe_4$. A possible reason for the difference is additional phonon scattering in the experimental samples due to point defects (especially Cu_{Hg} and Hg_{Cu} antisites in the quaternary) and grain boundaries.

Phase	β_p/β_{PbTe}	β_n/β_{PbTe}	$m^*_{b,VB}$ (m_e)	$m^*_{b,CB}$ (m_e)	$N_{b,VB}$	$N_{b,CB}$	κ_L (W/mK)	μ_h (cm^2/Vs)	μ_e (cm^2/Vs)
Hg_2GeTe_4	0.3	1.2	0.49	0.01	2	1	1.1	20	770
$Cu_2HgGeTe_4$	0.4	3.8	0.35	0.02	3	3	5.9*	28	3050

6. Material parameters used in AMSET calculation for electronic transport properties

Table S2: Materials parameters used to compute scatterings rates. C is the elastic tensor in Voigt notation, in units of GPa. ϵ_s and ϵ_∞ are the static and high-frequency dielectric constants. E_d^{VBM} and E_d^{CBM} are the absolute deformation potentials at the valence and conduction band edges, respectively. ω_{po} is the effective polar phonon frequency given in THz. For all tensor properties, components that are not explicitly listed are zero.

	ASMET input material parameters										
Compound	ϵ_s	ϵ_∞	E_d^{VBM}	E_d^{CBM}	ω_{po}	C_{11}	C_{22}	C_{33}	C_{44}	C_{55}	C_{66}
Hg_2GeTe_4	12.0	10.6	2.8	5.3	5.1	38.9	38.9	32.4	23.4	14.3	14.3
$Cu_2HgGeTe_4$	11.4	11.2	2.7	5.8	2.5	63.6	63.6	60.1	28.0	27.3	27.3

7. AMSET calculations for scattering types

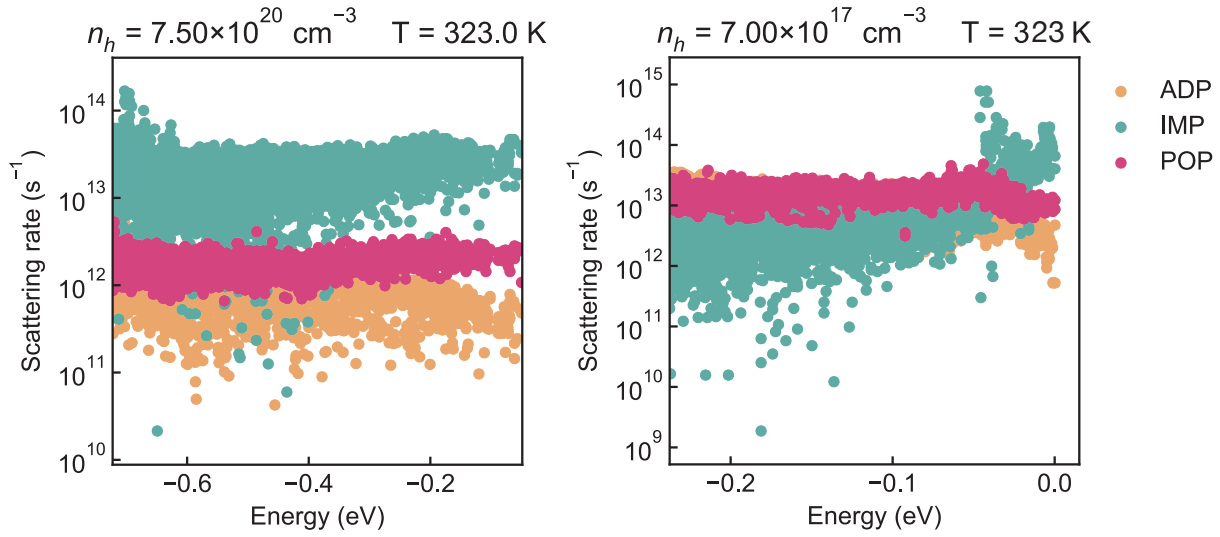

Figure S5: Electron scattering rate for $Cu_2HgGeTe_4$ (left) and Hg_2GeTe_4 (right) calculated by AMSET. The dominant scattering type for both materials is ionized impurity (IMP) scattering while polar-optical phonon (POP) and acoustic deformation potential (ADP) scattering also play a significant role.

8. Goldsmid Sharp band gap for Hg_2GeTe_4

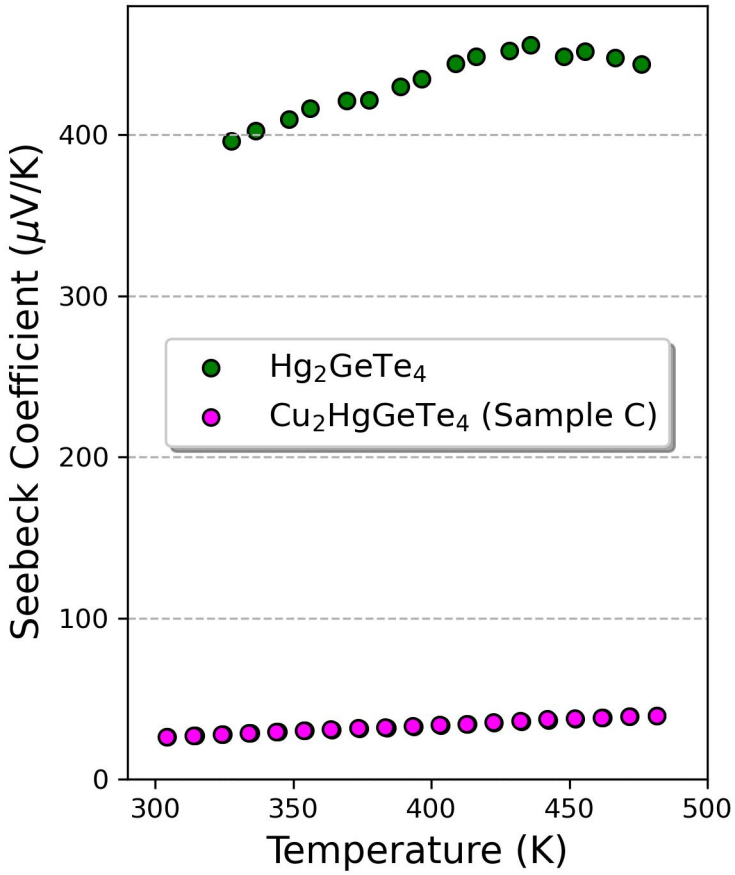

Figure S6: Seebeck coefficient measured from 50 to 200°C for sample Hg_2GeTe_4. The Goldsmid Sharp band gap[2] ($E_g = 2e|\alpha_{max}|T_{max}$) is calculated from the maximum Seebeck coefficient obtained for the sample: 460μV/K (at 160°C). Seebeck coefficients for Sample C (corresponding to point C of our phase boundary mapping) are low, barely increasing, and due to the degenerate carrier concentration, unlikely to exhibit a rollover in carrier type before the sample melts. Therefore, the Goldsmid Sharp band gap cannot be computed for the quaternary but data are shown to illustrate the contrast between the intrinsic ternary and degenerate quaternary compounds.

9. Temperature Dependent Hall Mobility (μ_H)

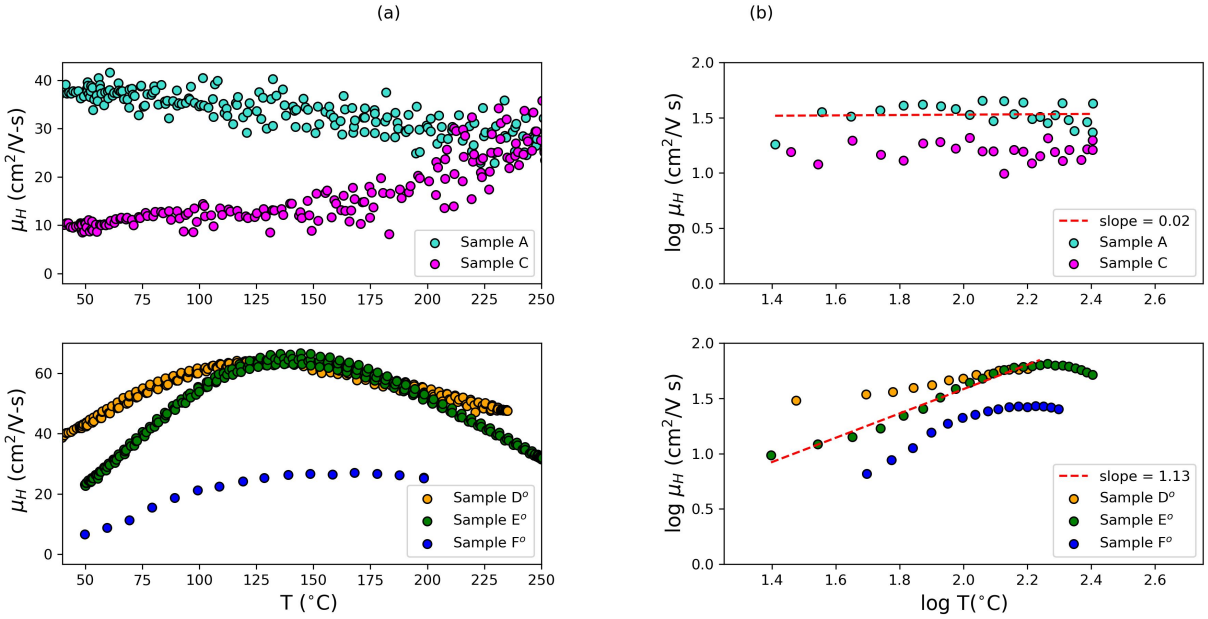

Figure S7: Temperature-dependent Hall mobility shown for quaternary (top plots) and ternary samples (bottom plots). Sample B omitted due to data flipping sign from negative to positive, which is likely a result of erroneous instrument signal noise at very high sample carrier concentrations (>10^{21} carriers/cm^3) rather than evidence of bipolar behavior. Between the temperatures of 50-150°C the ternary exhibits a marked increase in mobility with temperature due to ionized impurity scattering. A combination of acoustic phonon and ionized impurity scattering is assumed for the quaternary. Higher carrier concentration samples (Sample C for $Cu_2HgGeTe_4$, Sample F^0 for Hg_2GeTe_4) exhibit lower mobility, likely due to their increased defect concentration of vacancies, which serve as scattering sites.

To determine the scattering parameter r for Hg_2GeTe_4 and $Cu_2HgGeTe_4$, we analyzed the behavior of temperature-dependent Hall mobility. For the ternary, mobility rises with temperature, and the slope of the plotted log μ_H as a function of log T yields 1.13, in acceptable agreement with the relation $\mu_I \approx T^{3/2}$ for ionized impurity scattering(IMP).[3,4] The quaternary exhibits no such rise in mobility with temperature, suggesting that another scattering regime besides IMP is present. Neutral impurity scattering (point defect scattering) is unlikely to play a role since all neutral defects in both compounds are much higher in energy than charged defects (Figure 4 in main text). Hence, we assert that acoustic phonon (ADP) scattering accompanies IMP scattering in $Cu_2HgGeTe_4$. The associated r values for IMP and ADP are 1.5[3,4] and -0.5;[5] for Hg_2GeTe_4 we select an r value of 1.5 and for $Cu_2HgGeTe_4$ we select an r value of 1 because we simply consider the addition of r values for ADP (r= -0.5)[4] and IMP (r= 1.5).[3,5] We admit that the linear addition of r values is a crude method, but we observe excellent agreement between experimental and theoretical m^*_{DOS} and logical positions of E_F using this estimate.

10. Experimental Effective Mass (m^*_{DOS}) and Fermi Energy (E_F)

Table S3: Reduced chemical potential (η), E_F, and m^*_{DOS} for $Cu_2HgGeTe_4$ (Samples A-C) and Hg_2GeTe_4 (Samples D^0-F^0)

Sample	Scattering Regime	η	E_F	m^*_{DOS}
A	IMP/ADP	22.66	0.63	0.36
B	IMP/ADP	75.82	2.12	0.55
C	IMP/ADP	20.81	0.58	0.54
D^0	IMP	0.724	0.02	0.14
E^0	IMP	-0.29	-0.01	0.15
F^0	IMP	0.122	0.00	0.36

Scattering regimes for the quaternary include ionized impurity (IMP) and acoustic phonon (ADP) scattering. IMP scattering regime is chosen for the ternary (see Section 9 above for explanation). E_F is calculated by multiplying η by k_BT, which equals 0.028 eV at 50°C. Note that a negative value of η or E_F signifies position above the valence band (within the bandgap) whereas a positive value denotes position within the valence band. Reduced chemical potential and m^*_{DOS} are calculated using a Python script that assumes a single parabolic band (SPB) model and requires scattering parameter r, Hall carrier concentration, and Seebeck coefficient as inputs. The script back-solves for η using equations from Boltzmann transport theory.[6] These values were calculated at 50°C.

The experimental effective mass values reported in the main text (m^*_{DOS} for $Cu_2HgGeTe_4 = 0.49$ and m^*_{DOS} for $Hg_2GeTe_4 = 0.21$) were obtained by averaging the three values for each compound (A-C for the quaternary, for example) from the table above to obtain a single effective mass value for the ternary and a single value for the quaternary for easier comparison with the electronic calculated effective mass.

11. Electronic structures for $Cu_2HgGeTe_4$ and Hg_2GeTe_4 (HSE06)

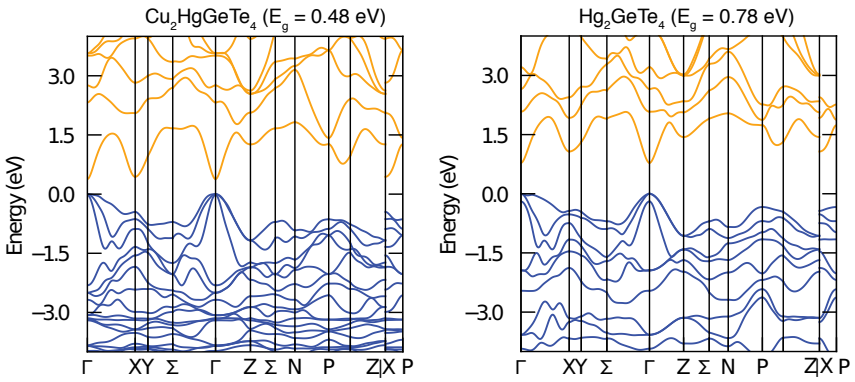

Figure S8: Electronic band structure of $Cu_2HgGeTe_4$ (left) and Hg_2GeTe_4 (right) along the special k-point path of the Brillouin zone, calculated from HSE06 hybrid functional. Electronic structures are plotted using Sumo[1] python toolkit.

12. Visualization of Cu interstitial sites in $Cu_2HgGeTe_4$ and Hg interstitial sites in Hg_2GeTe_4

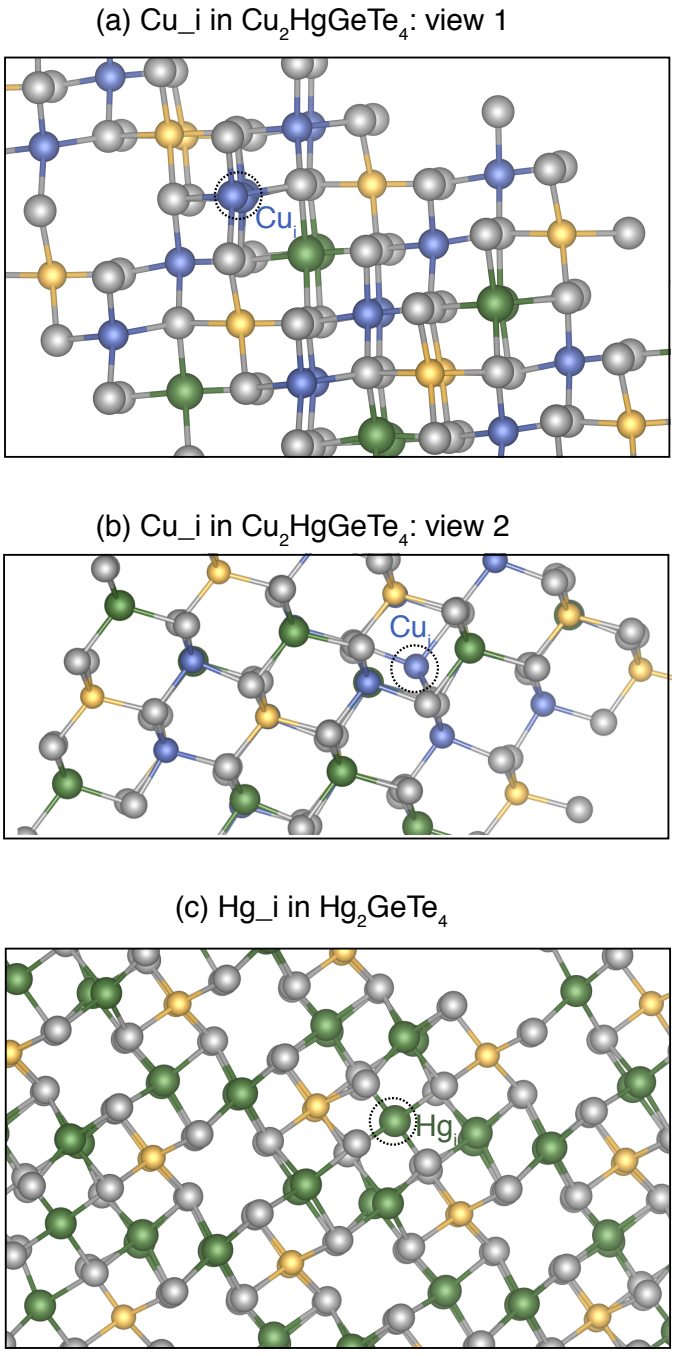

Figure S9: Structures of energetically favorable interstitial sites in $Cu_2HgGeTe_4$ and Hg_2GeTe_4. The intersitials sites are determined using a Voronoi tessellation scheme as implemented in the pylada-defects [7] software package.

13. Temperature dependent carrier concentration

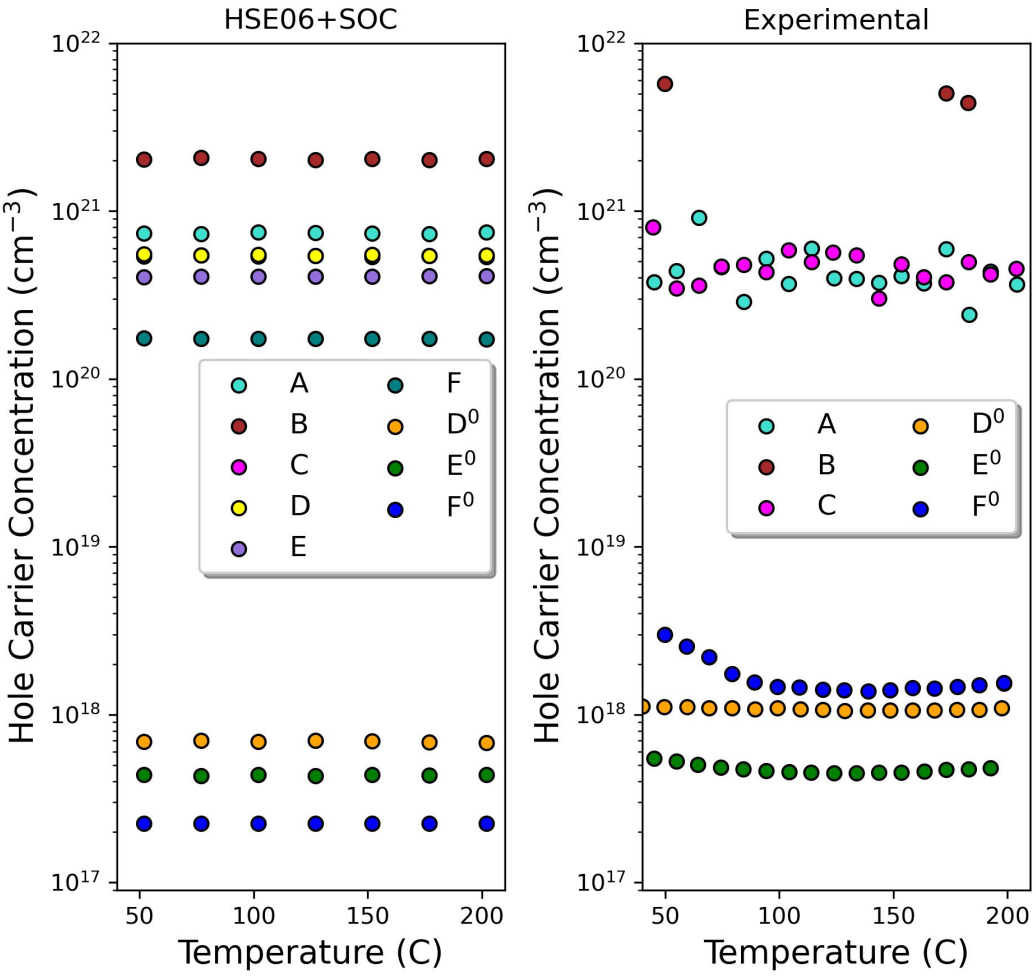

Figure S10: Left plot shows calculated carrier concentration for all phase boundary mapped (PBM) points A-F ($Cu_2HgGeTe_4$) and D^0-F^0 (Hg_2GeTe_4) (see **Fig 2** for description). The data for PBM C are so close to PBM D that the points are hidden. Right plot shows measured carrier concentration for PBM points A-C and D^0-F^0 (Recall that points D-F are impossible to synthesize due to the formation of an alloy between Cu/Hg_2GeTe_4). Only some experimental data for sample PBM B are shown because at high carrier concentration ($>10^{21}$ carriers/cm^3) our Hall instrument erroneously reports negative and positive values for carrier concentration due to the Hall coefficient going to zero. We report positive values in which we are confident.

14. Temperature dependent electrical conductivity

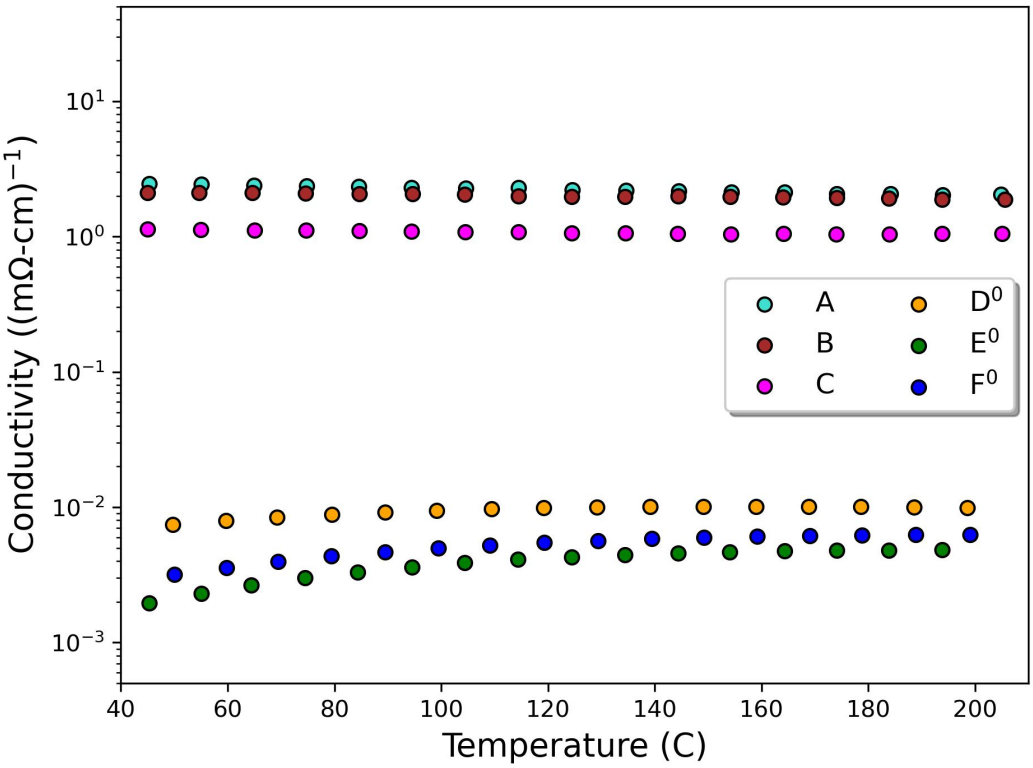

Figure S11: Experimental electronic conductivity for phase boundary mapped (PBM) samples A-C ($Cu_2HgGeTe_4$) and D^0-F^0 (Hg_2GeTe_4). Each letter corresponds to a corner on the chemical potential space polyhedron of phase stability established in the main text (**Fig 2**). Note that PBM A and B have nearly identical conductivity, but PBM B has higher carrier concentration (**Fig S11**). PBM A has higher mobility than PBM B (at 50°C, 30 vs 6 cm^2/Volt-sec, respectively), which explains this discrepancy.

References

(1) Ganose, A. M.; Jackson, A. J.; Scanlon, D. O. sumo: Command-line tools for plotting and analysis of periodic* ab initio* calculations. *Journal of Open Source Software* **2018**, *3*, 717.

(2) Gibbs, Z. M.; Kim, H.-S.; Wang, H.; Snyder, G. J. Band gap estimation from temperature dependent Seebeck measurement—deviations from the 2e— S— maxTmax relation. *Applied Physics Letters* **2015**, *106*, 022112.

(3) Debye, P.; Conwell, E. M. Electrical properties of n-type germanium. *Physical Review* **1954**, *93*, 693.

(4) Xie, H.; Wang, H.; Fu, C.; Liu, Y.; Snyder, G. J.; Zhao, X.; Zhu, T. The intrinsic disorder related alloy scattering in ZrNiSn half-Heusler thermoelectric materials. *Scientific reports* **2014**, *4*, 1–6.

(5) Ahn, K.; Li, C.-P.; Uher, C.; Kanatzidis, M. G. Thermoelectric properties of the compounds AgPb m LaTe m+ 2. *Chemistry of Materials* **2010**, *22*, 876–882.

(6) Shen, J.; Chen, Z.; Zheng, L.; Li, W.; Pei, Y., et al. Single parabolic band behavior of thermoelectric p-type CuGaTe 2. *Journal of Materials Chemistry C* **2016**, *4*, 209–214.

(7) Goyal, A.; Gorai, P.; Peng, H.; Lany, S.; Stevanovic, V. A computational framework for automation of point defect calculations. *Comp. Mater. Sci.* **2017**, *130*, 1.